ARTICLE   OPEN

Check for updates

Noninvasive imaging of 4D electrical activation patterns of uterine peristalsis during normal menstrual cycles

Sicheng Wang[1,2,3,7], Kelsey Anderson[3,4,7], Stephanie Pizzella[2,3], Haonan Xu[2,3], Wenshang Wang[1], Zichao Wen[2,3], Yuan Nan[2,3], Josephine Lau[2,3], Qing Wang[5], Valerie Ratts[3,4 ✉] and Yong Wang[2,3,5,6 ✉]

Uterine peristalsis, characterized by spontaneous slow-wave contractions of the subendometrial layer of the uterine myometrium, occurs throughout the menstrual cycle. Disruptions in peristalsis patterns may occur in women experiencing abnormal uterine bleeding, endometriosis, and infertility. Current tools to measure uterine peristalsis in humans have limitations that hamper their research or clinical utility. Here, we developed an electrophysiological imaging system with wearable electrical sensors to noninvasively quantify the four-dimensional electrical activation pattern during human uterine peristalsis with high spatial and temporal resolution and coverage. To demonstrate capabilities of this new imaging system, we enrolled 26 pre-menopausal participants ages 18–40 years old with regular menstrual cycles (25–34 days in length) and normal gynecologic anatomy. Participants initially underwent magnetic resonance imaging to obtain the body-uterus geometry. Then, during each of the four phases of a single menstrual cycle, patients underwent noninvasive electrical recording for 30 min. We measured uterine peristalsis frequency, direction, duration, magnitude, and power and found that these parameters differed in different phases of the menstrual cycle. Future use of this uterine peristalsis imaging system may advance our understanding of the role of uterine peristalsis in maintaining normal uterine function and contributing to gynecological pathophysiology.

INTRODUCTION

During each of the four phases of the human menstrual cycle, the subendometrial layer of the uterine myometrium generates slow, low-magnitude, spontaneous contractions termed uterine peristalsis[1–10]. During the menses phase, peristalsis waves primarily propagate from the fundus to the cervix (F–C), aiding the expulsion of blood and tissue. In contrast, during the peri-ovulatory phase, peristalsis waves predominantly propagate from the cervix toward the fundus (C–F) and are thought to help transport sperm toward the fallopian tubes.

Using transvaginal ultrasound (TVUS), Ijland et al. detected uterine peristalsis waves traveling C–F and others traveling F–C[11,12]. TVUS has a few limitations. First, TVUS requires insertion of a vaginal probe, which can be uncomfortable for the participant. Second, the quality of TVUS images may be limited by the position and orientation of the uterus. Third, traditional visual inspection of TVUS video is sometimes subjective and operator dependent, causing limited interobserver agreement in determining peristalsis direction[13]. Therefore, TVUS may result in incomplete findings[14–19]. Recent developments of quantitative video analysis like strain analysis[20,21] and speckle tracking[22–24] can generate quantitative measures.

Other methods that have been used to study uterine peristalsis also all have significant limitations. Intrauterine pressure catheters are invasive, and a catheter placed inside the uterus could alter peristalsis patterns. Hysterosalpingography cannot be used to measure peristalsis amplitude or frequency, and radiation exposure limits the imaging duration. Cine magnetic resonance imaging (MRI)[25–28] can be used to detect uterine peristalsis by acquiring sequential images over time and playing the MRI frames at elevated speed[25]. However, extended cine MRI is expensive, time-consuming, and operator-dependent, and it cannot reveal the initiation and termination sites of uterine peristalsis. Moreover, all these modalities can be uncomfortable for the participant and cannot be used for long-term observation.

An alternative technique for evaluating uterine peristalsis is to record the slow-wave electrical signals that drive contractions. For example, Kuijsters et al.[7] measured spontaneous electrical signals in ex vivo human uteri. In another study, electrodes were placed inside the nonpregnant uterine cavity to directly measure electrical activity on the uterine surface[29]. Additionally, Sammali et al.[30] used transabdominal electromyography to measure uterine electrical activity from electrodes placed on the body surface. However, this method only captures high-frequency electrical signals from a small abdominal area, so it cannot characterize the spatial patterns of peristalsis on the uterine surface. A new method is needed to noninvasively and quantitatively define the detailed features of human uterine peristalsis over the entire uterus for an extended period of time.

We recently developed an electrophysiological imaging system called electromyometrial imaging (EMMI)[31–34] to quantitate the electrical activity underlying uterine contractions during labor. Herein, we adapted EMMI to develop a new uterine peristalsis imaging (UPI) system and used it to longitudinally image the four-dimensional (4D) electrical activation patterns of uterine peristalsis over each phase of the menstrual cycle in healthy, nonpregnant participants with normal menstrual cycles. With UPI, we provide quantitative evidence that uterine peristalsis changes in

[1]Department of Electrical and Systems Engineering, Washington University in St. Louis, St. Louis, MO 63130, USA. [2]Center for Reproductive Health Sciences, Washington University in St. Louis, St. Louis, MO 63108, USA. [3]Department of Obstetrics & Gynecology, Washington University in St. Louis, St. Louis, MO 63108, USA. [4]Division of Reproductive Endocrinology & Infertility, Washington University in St. Louis, St. Louis, MO 63108, USA. [5]Mallinckrodt Institute of Radiology, Washington University in St. Louis, St. Louis, MO 63110, USA. [6]Department of Biomedical Engineering, Washington University in St. Louis, St. Louis, MO 63130, USA. [7]These authors contributed equally: Sicheng Wang, Kelsey Anderson. ✉email: valerie.ratts@wustl.edu; wangyong@wustl.edu

Table 1. Demographics of enrolled patients ($N = 26$) with regular menstrual cycles.

Age, years	27.75 (25.96–29.54)			
Body mass index, kg/m^2	29.99 (26.82–33.18)			
Race, n (%)				
White	14 (53.8%)			
Black	9 (34.6%)			
Asian	2 (7.7%)			
Other	1 (3.8%)			
Cycle length, days	28.35 (27.46–29.24)			
Phase	Menses	Proliferative	Ovulatory	Secretory
Estradiol (pg/mL)	33.7 (27.0–40.4)	93.9 (76.7–111.1)	155.9 (119.3–192.6)	118.9 (99.7–138.2)
Progesterone (ng/mL)	0.28 (0.21–0.35)	0.20 (0.20–0.21)	2.00 (1.20–2.80)	8.34 (6.52–10.16)
Endometrial thickness (mm)	3.50 (2.66–4.34)	6.79 (5.94–7.64)	8.92 (7.56–10.28)	9.43 (8.28–10.58)

Mean value and 95% confidence interval are shown for each numerical variable.

frequency, direction, duration, magnitude, and power throughout the menstrual cycle.

RESULTS

Study participants

We enrolled 26 non-pregnant pre-menopausal women between 18 and 40 years of age who were not using hormonal medication and had regular menstrual cycles between 25 and 34 days in length. Demographic and gynecologic history data of enrolled participants are shown in Table 1.

Uterine peristalsis imaging (UPI) system

The UPI system is illustrated in Fig. 1. First while applying MRI-compatible fiducial markers around the abdomen and lower back, a participant undergoes a one-time, fast, anatomical MRI scan (Fig. 1A) to acquire the patient-specific uterus-body surface geometry (Fig. 1B, C). Second, at each phase of the menstrual cycle, customized wearable pin-type electrode patches are applied to the same locations on the body surface as the MRI fiducial markers (Fig. 1D). Body surface electrical signals (Fig. 1E) are recorded for 20–30 min, and electrical signals (Fig. 1F) are recorded with a band-pass filter (0.01–0.05 Hz)[19,35,36]. Third, UPI software is used to map electrical signals to each point on the entire three-dimensional (3D) uterine surface (Fig. 1G, H). These electrical signals are used to derive activation sequences (Fig. 1I).

4D spatial-temporal quantification of uterine peristalsis patterns

Uterine isochrone maps (Fig. 2A) were generated according to the activation sequence (Fig. 1I). Uterine surface data were analyzed to generate uterine magnitude maps (Fig. 2B). Based on uterine isochrone maps, we defined the peristalsis wave direction (C–F, F–C, or others) and locations of the initiation and termination sites (cervix area, fundus area, and other areas) for each peristalsis wave. We then summarized the data for all peristalsis waves recorded during the entire imaging session (Fig. 2C–E) and generated distribution probability maps of the initiation (Fig. 2F) and termination (Fig. 2G) sites for C–F and F–C peristalses for the entire imaging session. See detailed descriptions in the Methods section.

UPI findings in a healthy participant with regular menstrual cycles

In Fig. 3, we present representative uterine peristalsis waves of a 32-year-old healthy participant. During the menses phase, 40.4% of waves traversed from near the fundus toward the cervix (F–C), and 25.5% traversed from near the cervix toward the fundus (C–F) (Fig. 3A). During the proliferative phase, 42.7% of waves were F–C and 36.5% were C–F (Fig. 3B). During the ovulatory phase, 45.2% of waves were C–F, and 33.3% were F–C (Fig. 3C). In the secretory phase, 41.9% of waves were C–F, and 32.6% were F–C (Fig. 3D). In all cases in which we were able to determine the direction of peristalsis in TVUS images ($n = 88/94$, 93.6% of waves), the direction of peristalsis imaged by UPI matched the direction observed by TVUS.

Uterine peristalsis wave features differ by menstrual cycle phase in healthy participants

We used the UPI system to image uterine peristalsis in 26 healthy nonpregnant females with regular menstrual cycles. Electrical recording was conducted during each menstrual cycle phase, and all data for each phase from all 26 participants were compiled. We first plotted the frequency of peristalsis waves by days in a standard 28-day menstrual cycle (Fig. 4A). On average, frequency peaked around day 15 (during the periovulatory phase). Next, we plotted the average peristalsis wave frequency (Fig. 4B) during each phase and saw that the highest frequency (3.13 [2.72, 3.54]) occurred in the periovulatory phase, and the lowest frequency (1.43 [1.21, 1.67]) occurred in the menses phase. Plotting the average direction ratios revealed that the most common wave directions were C–F or F–C (Fig. 4C–E). Plotting the average magnitude (Fig. 4F–H) revealed that the C–F and F–C waves had higher magnitudes than the other direction waves. The highest magnitude C–F waves were in the periovulatory phase (Fig. 4F), and the highest magnitude F–C waves were in the menses phase (Fig. 4G). Finally, we plotted average power (Fig. 4I–K) and found that the highest power C–F waves were during the periovulatory phase (Fig. 4I) and that the highest power F–C waves were during the menses phase (Fig. 4J).

Asymmetric C–F peristalsis direction correlates with dominant follicle in the periovulation phase

We noticed that C–F peristalsis waves during the peri-ovulatory phase tended to move preferentially toward one fallopian tube. In Fig. 5A–C, we present data from one participant whose dominant follicle was on the right side. Figure 5A displays a T2-weighted anatomical scan focusing on the pelvic region and reproductive
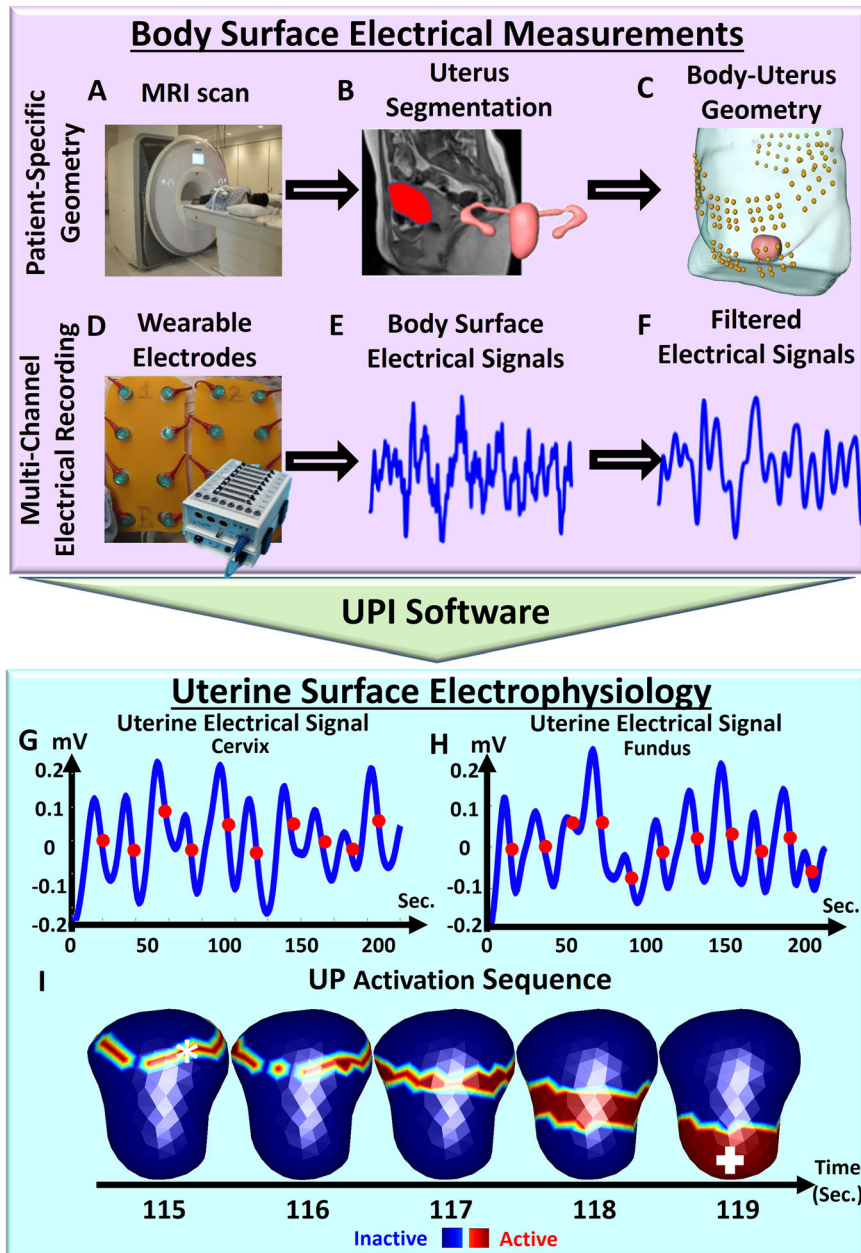
Fig. 1 Schematic of uterine peristalsis imaging system. Anatomical MRI (**A**) followed by segmentation (**B**) yields a patient-specific geometry of the body surface, uterus surface, and fallopian tubes (**C**). Yellow dots indicate positions of MRI-compatible markers. **D** Electrode patches are placed on the participant's abdomen and back in the same positions as the markers. Raw (**E**) and filtered (**F**) electrical signals (bandwidth: 0.01–0.05 Hz). Uterine surface electrical signals from (**G**) one uterine surface point near the cervical region (white plus sign in (**I**)) and (**H**) one uterine surface point around the fundal region (white asterisks in (**I**)). Red dots denote the points of steepest negative slope to represent the activation times during peristalsis cycles. **I** Detailed activation sequence of one complete uterine peristalsis wave initiated near the fundus and terminated near the cervix. Blue indicates inactive uterine regions, and red indicates active uterine regions.

organs, and Fig. 5B shows the reconstructed 3D uterus geometry. Figure 5C illustrates sequential isochrone maps of asymmetric C–F peristalses, with red indicating the initiation sites and blue indicating the termination sites. All three of these peristalsis waves traveled toward the right follicle.

For 15 participants, we were able to determine by TVUS which ovary had a dominant follicle. The clinical characteristics and measurements of these patients are summarized in Table 2. For each of these participants, we created maps illustrating the probability of C–F peristalsis waves during the periovulatory phase terminating in a particular region. Figure 5D exhibits the termination probability maps of five participants with right-sided

dominant follicles. Figure 5E displays the termination probability map of ten participants with left-sided dominant follicles. In most cases, the most common termination sites (red in the maps) were on the side closest to the ovary containing the dominant follicle.

DISCUSSION

The UPI system presented here can noninvasively and objectively provide detailed information about the electrical activation patterns of uterine peristalsis at high spatial and temporal resolution. In all phases of the menstrual cycle, the most common directions of uterine peristalsis waves were C–F and F–C, but we
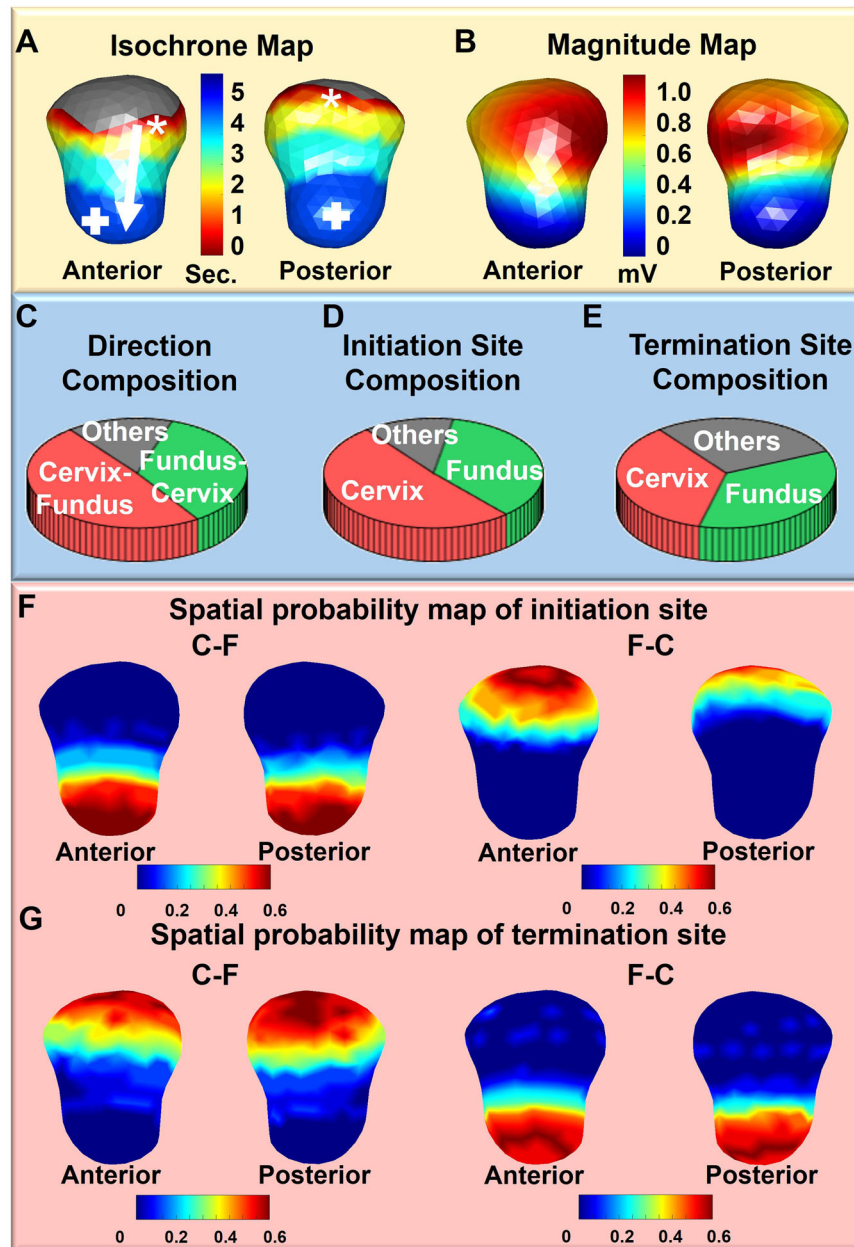
Fig. 2 Quantification of uterine peristalsis waves. A Uterine isochrone maps from the same uterine peristalsis wave as in Fig. 1I. Warm and cool colors represent early and late activation, respectively. The white arrow depicts the peristalsis wave propagation direction. **B** Uterine magnitude map from the same uterine peristalsis wave in Fig. 1I, showing the magnitude distribution over the entire 3D uterine surface in one peristalsis wave. **C** Distribution of uterine peristalsis directions (C–F, F–C, others) and initiation (**D**) and termination (**E**) sites (cervix, fundus, and other areas) analyzed from the entire electrical recording. Initiation (**F**) and termination (**G**) site distribution probability maps of C–F and F–C uterine peristalses for the entire imaging session (see details in Materials and Methods).

also observed other complex wave patterns as have been noted previously[12,13]. In these normal participants, the predominant peristalsis pattern in menses was F–C. Others have seen this pattern in TVUS and postulated that it facilitates expulsion of menstrual and endometrial tissue while protecting against ascending pathogens[37]. Inefficient F–C peristalsis waves may lead to accumulation of endometrial tissues in the uterine cavity and increase the risk of developing endometriosis.

We observed no dominant contraction pattern during the proliferative phase. Prior studies have shown that, in the late proliferative phase, the predominant peristalsis direction switches from F–C to C–F. We only performed electrical recording on

participants at one time in the proliferative phase and thus likely included data from both before and after this switch[38].

In the peri-ovulatory phase, the predominant peristalsis pattern was C–F. Kunz et al. used serial hysterosalpingography to follow labeled macrospheres the size of sperm and observed that they were transported from the cervix into the uterus and fallopian tubes[39], suggesting that the C–F peristalsis pattern facilitates the transport of sperm toward the oocyte. Consistent with this idea, we observed that C–F peristalsis waves commonly traveled in the direction of the dominant follicle.

Finally, in the secretory phase, we observed both C–F and F–C peristalsis waves, with neither predominating. This is consistent
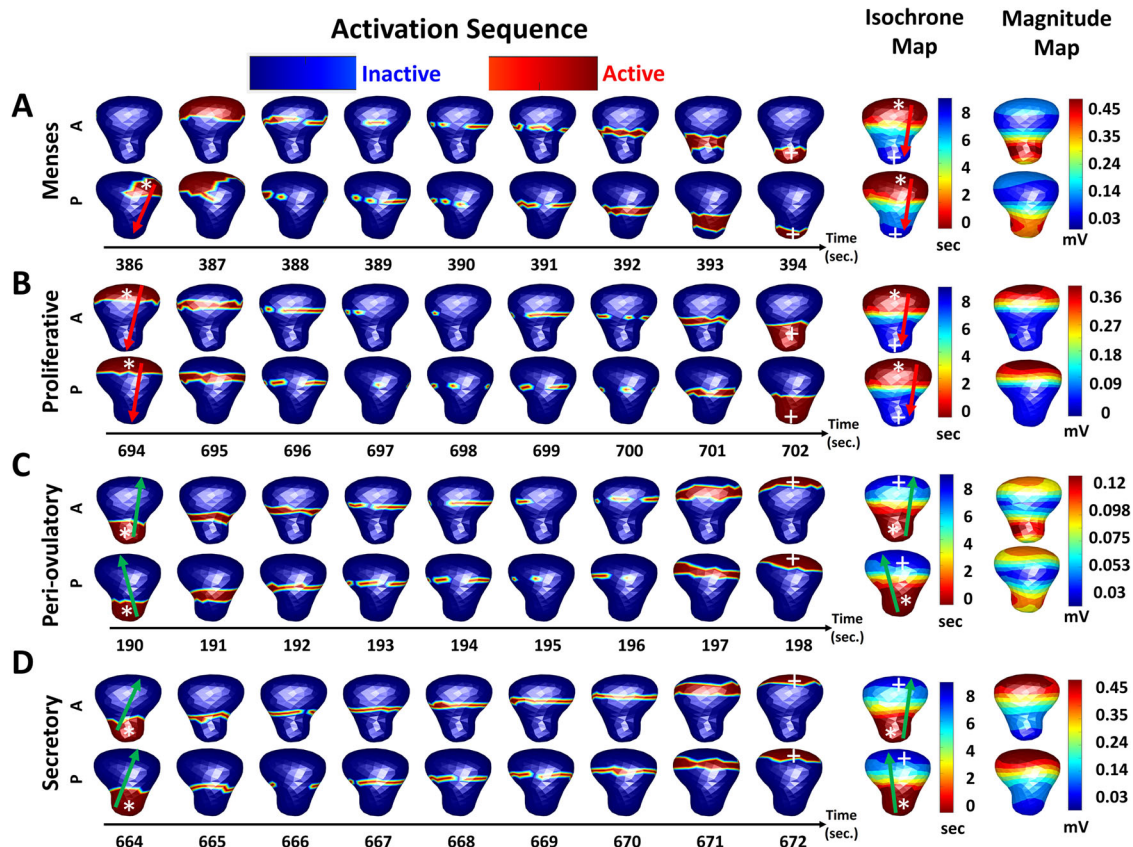
Fig. 3 Representative uterine peristalsis imaging (UPI) outcome in one healthy participant with normal menstrual cycles during four phases of the menstrual cycle. Dominant F–C uterine peristalsis pattern during the (**A**) menses phase and (**B**) proliferative phase. C–F uterine peristalsis patterns during the (**C**) peri-ovulatory phase and (**D**) secretory phase. In each panel, A represents the anterior view and P represents the posterior view of the uterus. White asterisks denote initiation sites, white plus signs denote termination sites, red arrows indicate F–C peristalsis waves, and green arrows indicate C–F peristalsis waves.

with work by Fanchin et al. [40] evaluating peristalsis waves at the time of embryo transfer after in vitro fertilization.

UPI has several technical advantages over other modalities used to image uterine peristalsis. First, UPI is noninvasive, which is optimal for long-duration uterine monitoring. Whereas we continuously recorded for up to 30 min, researchers using other modalities usually recorded for 5 min and at most 15 min. We are currently developing wearable electrode sensors, which would allow researchers to monitor uterine peristalsis for hours or days. Longer recordings will likely yield more accurate assessment of uterine peristalsis waves and permit identification of more complex wave patterns. Second, modalities using invasive monitoring may perturb peristalsis. For example, the TVUS probe touches the cervix, which could alter peristalsis. Third, UPI provides high spatial and temporal resolution and coverage and can characterize the complex patterns of electrical activation across the entire uterus. Thus, we are able to objectively measure the initiation sites, direction, frequency, and duration of uterine peristalsis waves. Finally, UPI data reflect participant-specific uterine-body anatomy uterine peristalsis patterns.

One limitation of our study is that a few enrolled participants may have had undiagnosed gynecologic pathology. We minimized this possibility by collecting detailed obstetric and gynecologic history from prospective participants during the screening process and excluding anyone with a history of uterine anomalies, infertility, ovulatory dysfunction, medication use, endometriosis, or documented fibroids greater than 3 cm. Nevertheless, future studies could expand the sample size and enroll more patients with recent gynecologic exams.

A second limitation is that the inverse calculations in the UPI software assume that the medium is homogeneous between the uterine surface and abdominal surface without any primary electrical source. However, the uterus in a non-pregnant person is near the bladder and bowel, both of which contain smooth muscles that generate slow-wave signals. Electrical signals from these organs are unlikely to interfere with our measurements for three reasons. First, the rhythmic phasic contractions are 0.33 Hz in human stomach, about 0.083 Hz in duodenum, and 0.125–0.167 Hz in ileum. As our band-pass filter selected activity between 0.01 and 0.05 Hz, none of these signals affected our analysis. Second, the detrusor muscle in the human bladder generates low-amplitude rhythmic contractions at 0.033 ± 0.008 Hz. Although this is within the frequency range for uterine peristalsis, participants were asked to empty their bladders before the study. Thus, the detrusor muscle was likely relaxed in our participants. Third, the electrical amplitude of slow-wave contractions in human bladder is low. Moreover, we validated over 90% of uterine peristalsis wave directions in simultaneously collected TVUS videos in each participant.

We are pursuing multiple avenues to further develop UPI. We aim to replace the current short anatomical MRI with a low-cost 3D ultrasound measurement to generate patient-specific body-uterus geometry. We also aim to refine the electrode placement to improve imaging accuracy and develop automatic or semi-automatic peristalsis wave classification. Finally, we are developing low-cost wearable electrode sensors[41,42]. Together, these technical advances will reduce the cost of the UPI system and make it easier to implement in a variety of settings.
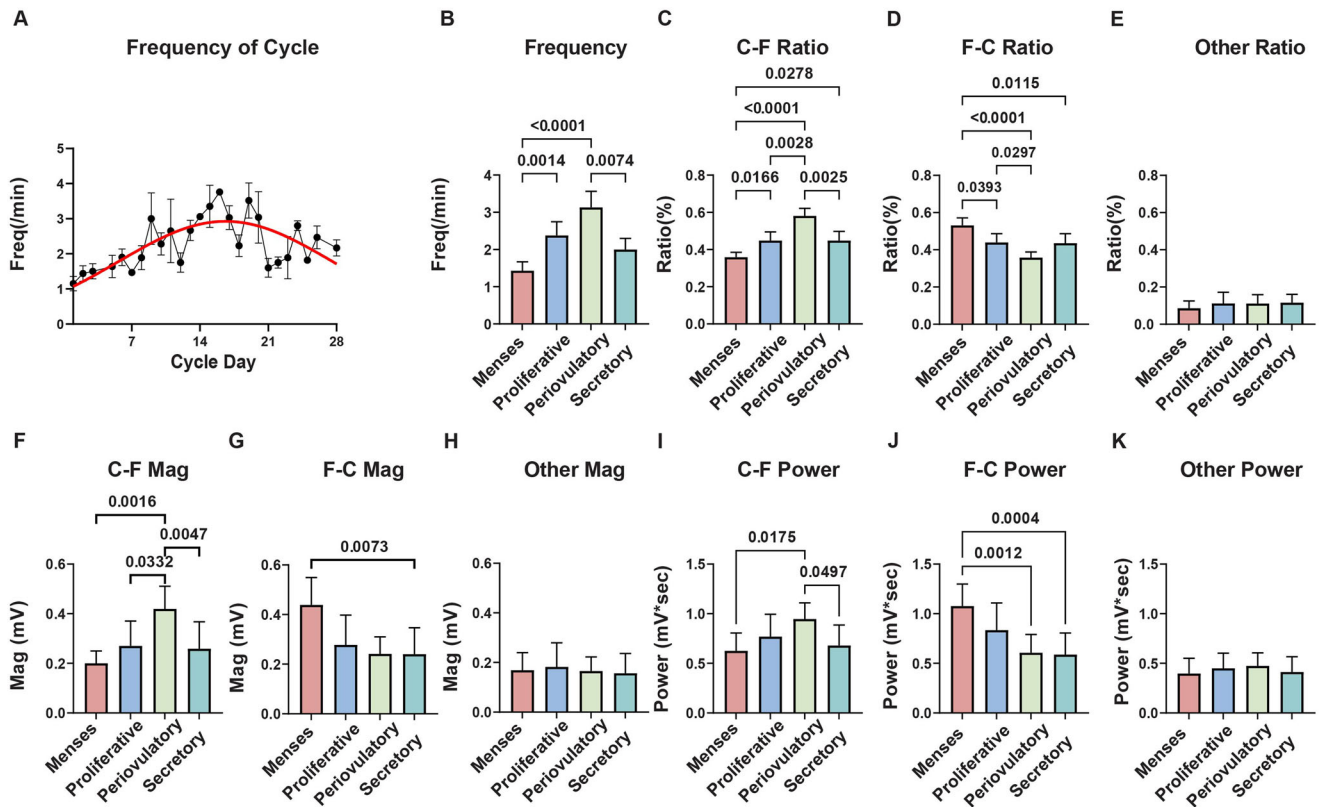
Fig. 4   Quantitative analysis of uterine peristalsis during each phase of the menstrual cycle. A Uterine peristalsis frequency plotted by day in a 28-day menstrual cycle. Red curve was fitted by using Gaussian distribution. **B** Peristalsis frequency during the four phases. **C, D, E** Direction ratio of peristalsis waves in C–F, F–C, and other directions. **F, G, H** Magnitude of uterine peristalsis waves in C–F, F–C, and other directions. **I, J, K** Power of peristalsis waves in C–F, F–C, and other directions. $N = 26$ participants in each phase. Error bars in (**A**) depict the 95% confidence interval. Column bars in (**B–K**) are shown as mean values with 95% confidence interval. Kruskal-Wallis test was performed to analyze the difference of each UPI parameter between menstrual cycle phases. P-values less than 0.05 are marked.

In future larger studies, UPI can be used to establish reference ranges for features of uterine peristalsis in normal menstrual cycles. These normal reference ranges could be used to identify patients with abnormal gynecological conditions such as endometriosis, ovulatory dysfunction, uterine anomalies, abnormal uterine bleeding, and infertility. Moreover, with the detailed 4D electrical activation patterns imaged by UPI, it will be possible to longitudinally evaluate the effects of various clinical interventions and optimize treatment plans for individual patients. In the long term, UPI may facilitate development of nonpharmaceutical strategies to electrically correct abnormal uterine peristalsis underlying gynecological conditions such as endometriosis. This approach would be similar to how cardiac pacemakers are now used to treat heart conditions.

METHODS
Ethics and participant enrollment
This study was performed in the Division of Reproductive Endocrinology & Infertility and Center for Outpatient Health at Washington University School of Medicine. This study was approved by the Washington University Institutional Review Board, and all participants signed informed consent documents. Participants were included if they were female at birth, between the ages of 18 and 37 years, and had regular, predictable menstrual cycles every 24–35 days. Potential participants were excluded if they were post-menopausal, pregnant, or breastfeeding; had a uterine anomaly; had exposure to medications known to affect uterine contractility (e.g., magnesium, opioids, beta

antagonists, nifedipine); were non-English speaking; had abdominal circumference >55 cm; had MRI contraindications (pacemaker, metal implants, etc.); or had documented or self-reported histories of infertility, ovulatory dysfunction, or endometriosis. Each participant was imaged with the UPI system four times during one menstrual cycle, once each during menses, early proliferative, late proliferative (peri-ovulatory), and secretory phases.

Determination of phase in the menstrual cycle
Patients were determined to be in one of four menstrual phases (menses, early proliferative, late proliferative, and secretory) by using a combination of patient-reported bleeding, cycle length, ultrasound findings, ovulation predictor kit (Clearblue, Geneva, Switzerland) results, and hormonal measurements. Serum (5–10 ml) was collected and sent to the Core Laboratory for Clinical Studies at Washington University in St. Louis to measure concentrations of estradiol, progesterone, and testosterone. The menses phase was assigned when a patient reported bleeding. The early proliferative phase was assigned after the patient had stopped bleeding, ultrasound demonstrated early follicular activity (largest average follicle dimension <16 mm), serum estradiol <200 pg/ml, and serum progesterone <3 ng/ml. The late proliferative (peri-ovulatory) phase was defined by a positive result on an ovulation predictor kit, serum estradiol >200 pg/ml, serum progesterone <3 ng/ml, and/or a dominant follicle on ultrasound (largest average follicular dimension ≥16 mm). The secretory phase was assigned when serum progesterone was >3 ng/ml.

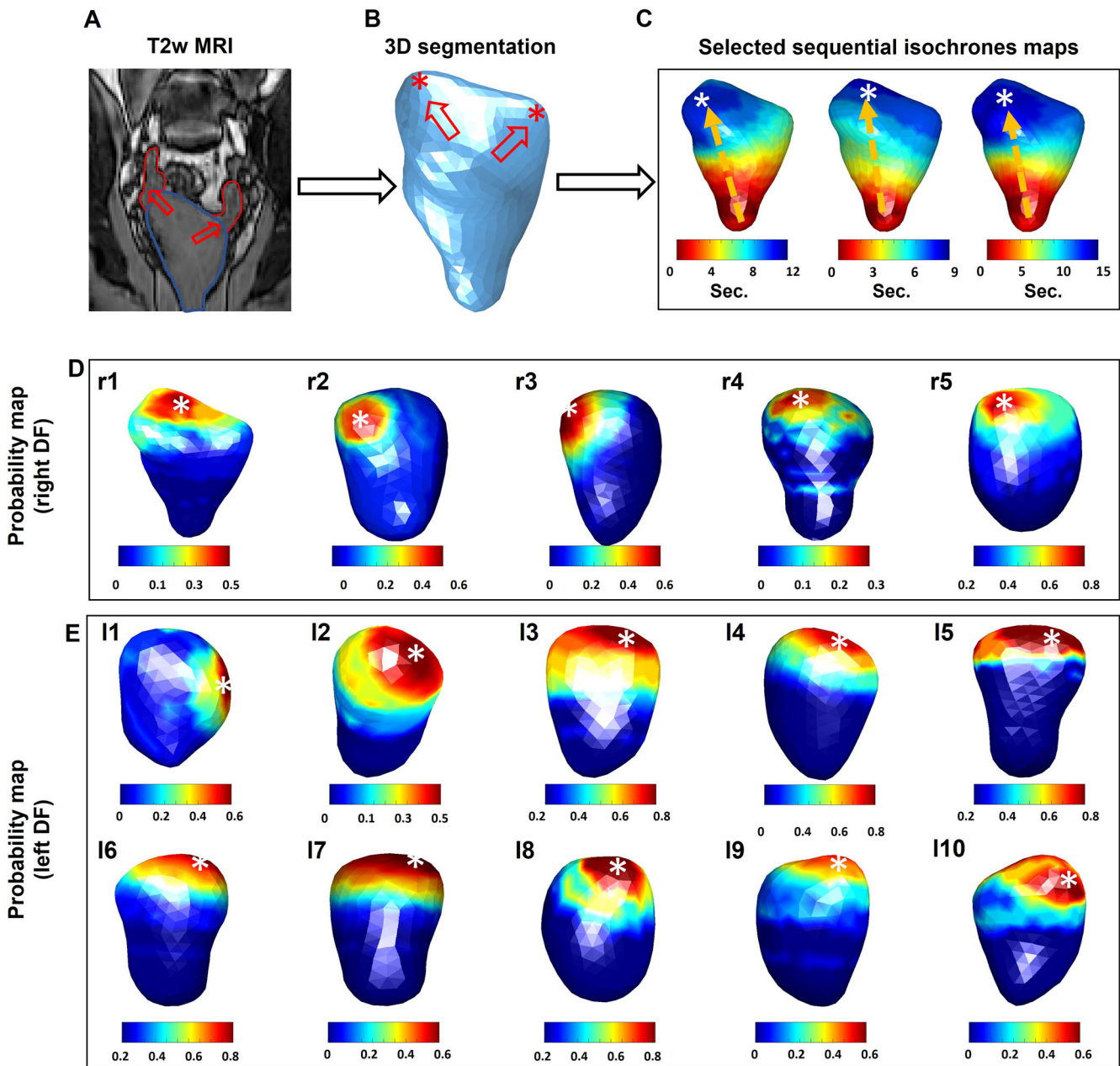**Fig. 5 Uterine peristalsis patterns during periovulation in participants with identified dominant follicles. A** T2-weighted anatomical image of one participant (r1) with right dominant follicle. Blue segment is the uterine cavity and red segments are the follicles. **B** Reconstructed 3D uterine geometry from the participant in (**A**) with two interstitial portions marked by red stars. **C** Three selected sequential isochrones maps from the participant in (**A**). Red indicates the initiation site, blue indicates the termination site, and the orange arrow indicates the peristalsis wave direction. Termination probability maps of five participants with right dominant follicle (**D**), and ten with left dominant follicle (**E**). All images show anterior views of the uterus.

Uterine peristalsis imaging (UPI) procedure

First, a woman underwent a one-time, anatomical (T1W sequence) 3T Siemens Prisma MRI scan (~10 min) to acquire the patient-specific uterus-body surface geometry while wearing up to 10 patches containing up to 128 MRI-compatible fiducial markers around the abdomen and lower back (Fig. 1A). 3D uterus segmentation was performed in T1-weighted anatomical images using the software Amira 6.2.0 with the standard image processing procedure. Uterus and body geometry were generated, and electrode locations were identified on the MRI anatomical images (Fig. 1 B, C). Second, customized BioSemi pin-type electrode patches were applied to the same locations on the body surface as the MRI fiducial markers. An ADC box was used to record the body surface electrical signals (Fig. 1D, E) for 20 min. Third, the participant underwent another 10-min electrical recording while simultaneously undergoing transvaginal ultrasound (TVUS). TVUS scans of the uterus were performed by a sonographer holding the transducer probe while the patient was lying in a lithotomy position. After obaining anatomical images to inform menstrual phase determination, cine clips were recorded on a GE Voluson S8 ultrasound machine. The duration of each clip was 20 s and 30–35 clips were acquired, on average.

Table 2. Clinical characteristics and measurements in 15 participants with dominant follicles detected on ultrasound.

Patient ID	Age, years	Body mass index, kg/m^2	Gravidity	Cycle length, days	Dominant follicle	Diameters of largest average follicle (mm)
r1	32	48.7	0	28	Right	22.2, 18.5
r2	32	35.93	2	28	Right	19.9, 17.8
r3	32	24.51	0	28	Right	23.5, 15.3
r4	36	28.01	4	28	Right	21.0, 13.6
r5	25	27.96	0	28	Right	19.9, 19.1
l1	35	28.3	0	28	Left	19.9, 19.1
l2	25	26.73	0	27	Left	26.6, 22.6
l3	31	19.79	1	28	Left	23.8, 17.0
l4	30	38.4	0	31	Left	14.4, 18.7
l5	23	22.33	0	28	Left	23.8, 20.8
l6	26	26.93	0	28	Left	20.8, 18.6
l7	24	24.2	0	26	Left	22.0, 20.7
l8	29	34.67	3	27	Left	18.1, 12.4
l9	33	27.64	0	25	Left	11.4, 21.2
l10	21	22.24	0	27	Left	22.4, 18.1

High-density electrode patches

Specifically, the distance between electrodes is less than 1 cm, whereas it is more than 2 cm in the patches used for pregnant women. The electrode spatial density used to image the mild uterine peristalsis of the small nonpregnant uterus is more than four times higher than the version used to image the labor contractions from the large pregnant uterus. These high-density electrodes patches were placed around the participant's abdomen (front, back, and sides) to comprehensively capture the electrical signals from the uterine peristalses during menstrual cycles.

To enable the same patch placement across multiple visits, we employed multiple anatomical landmarks on the patient body surface to place adhesive rulers on patients' abdomen surface. The same electrode patches are placed at the same location along the rulers. As shown in Supplementary Fig. 1, four color-marked rulers are applied to the patient's front and back to establish the spatial coordinate system. There are a total of ten patches: four on the back, four on the front, and one on each side. Patches A1, A2, B1, B2 are placed on the patient's lower abdominal area. Patches C1 and C2 are placed on the patient's left and right sides of the abdomen. Patches D1, D2, D3, and D4 are placed on the patient's lower back. Specifically, we placed two adhesive rulers on the front (Supplementary Fig. 1A). One red ruler ran vertically along the umbilicus with the inferior end of the ruler ending at the superior edge of the patient's public symphysis. The inferior edge of the lower stomach patches (B1 & B2) are placed in line with the inferior end of the red vertical ruler. The patches are placed with the medial edge running along the red vertical ruler. Then, the green horizontal ruler is placed along the superior edge of the lower patches. The upper patches (A1 & A2) are placed above the horizontal ruler. Again, the patches are placed with the medial edge running along the vertical ruler. The side patches (C1 & C2) are placed with the inferior edge aligned with the top of the horizontal ruler from the front. Similarly, we placed two adhesive rulers on the back (Supplementary Fig. 1C). One organe ruler runs vertically along the spine with the inferior end of the ruler ending at the patient's coccyx. The purple horizontal ruler is placed at the top of the patient's hip bones. The patches (D1, D2, D3, and D4) are placed above the horizontal ruler. The medial patches are placed along the edge of the vertical ruler and the lateral patches (C1 & C2) are placed along the edge of the medial patches. The coordinates of each patch are also recorded in the longitudinal studies to further ensure the consistent placement of patches across multiple visits and avoid its influence on UPI results.

Signal processing

In experiments in which electrical signals were directly measured on the human nonpregnant uterine surface, the median uterine peristalsis frequency was 0.039 Hz in the proliferative phase and 0.020 Hz in the secretory phase[29]. In TVUS and cine MRI studies[1], the frequency of uterine peristalsis is between 0.33 and 6 contractions per minute throughout the cycle. Therefore, we selected a frequency band between 0.01 and 0.05 Hz[19,35,36] to minimize the high-frequency artifacts not correlated with electrical activities of uterine peristalsis. The body surface electrical signals were processed with a band-pass filter to generate wave electrical signals (peristalsis waves) over the entire abdomen surface (Fig. 1F).

Inverse computation in UPI

With the electro-quasi-static assumption of the bioelectric field, the inverse computation combines the patient-specific uterus-abdomen surface and electrical potentials measured on the abdominal surface to reconstruct the potential distribution over the entire 3D uterine surface. We assume that the medium is homogeneous between the uterine surface and abdominal surface without any primary electrical source. Then, the inverse problem could be mathematically described by the Cauchy problem for Laplace's Eq. (1) with boundary conditions (2, 3) on the abdominal surface.

$$\nabla^2 \phi(x) = 0 \qquad (1)$$

Dirichlet (2) and Neumann (3) conditions for the abdominal surface potentials are:

$$\phi(x) = \phi_{A(x)}, x \in \Gamma_A \qquad (2)$$

$$\frac{\partial \phi(x)}{\partial \boldsymbol{n}} = 0, x \in \Gamma_A \qquad (3)$$

Here, $\boldsymbol{n}$ is the normal vector on the abdominal surface at location x and Γ_A represents abdominal surface. $\phi_{A(x)}$ is the potential measured on the abdominal surface and $\phi(x)$ is the potential on the uterine surface.

Table 3. Endometrial wave classification system initially proposed by Ijland[11] and revised by Gestel[12].

Wave type	Wave symbol	Definition
Cervix–Fundus	C–F	Wave propagates from cervix to fundus
Fundus–Cervix	F–C	Wave propagates from fundus to cervix
Others	Alternating	Wave propagates from cervix to fundus with an alternating wave from fundus to cervix
	Recoiling	Wave propagates from cervix to fundus followed by a reflective wave toward cervix
	Standing	Visible wave with no propagation toward cervix or fundus
	Opposing	Wave start at cervical and fundal uterine regions simultaneously
	Random	Waves start at multiple sites on the uterus

As a mesh-free method robust to noise, a method of fundamental solutions[43] was deployed to discretize the Laplace's equation and boundary conditions, which is accurate for solving the bioelectric field inverse problem in both electrocardiographic imaging[43] and EMMI[31,33,34] systems. This problem cannot be solved directly as it is an ill-posed inverse problem. Therefore, Tikhonov-based inverse computation with a fixed regularization value of 0.01 was used to obtain the solution.

$$\Phi_A = \boldsymbol{A}\,\Phi_U \qquad (4)$$

Here, Φ_A is a $M * T$ matrix of measuring surface potentials, Φ_U is a $N * T$ matrix of uterine surface potentials, where M is the number of measuring electrodes applied on the abdominal surface and N is the number of discrete points on the uterine surface, and T is the number of recording time points. $\boldsymbol{A}$ is a $M * N$ linear transform matrix encoding the relationship between abdominal surface potential Φ_A and uterine surface potential Φ_U.

UPI data processing
The inverse computation described above was employed to compute the uterine surface electrical signals (Fig. 1G, H) on the 3D uterine surface. The times when the uterine surface electrical signals at various uterine surface areas reached the steepest negative slope[44–48] were extracted and defined as electrical activation times at those uterine areas during peristalsis waves (red dots in Fig. 1G, H). During each peristalsis wave, sequential time frames were generated as the activation sequences (Fig. 1I) to reflect the detailed 4D spatial-temporal activation patterns of the uterine peristalsis. Within each time frame, the red region indicated electrically activated myometrium areas currently experiencing peristalsis, and the blue region indicated inactive areas of the uterus. The isochrone map was generated as a color-coded 3D map to summarize the electrical activation sequence (Fig. 1I). In the isochrone map, warm and cool colors denote regions of the uterus that activated early and late, respectively, during the peristalsis wave.

Inspection of uterine peristalsis direction
Uterine peristalsis direction was categorized according to the wave classification system proposed by Gestel et al.[12] (Table 3). A customized UPI post-analysis software with graphical user interface was developed in MATLAB (R2021b) to visualize each peristaltic wave. The software first detected the uterine peristalsis waves according to the electrical activations and recorded the start and end times. Next, five independent observers visually inspected the electrical activation sequences and isochrone maps to define the direction, initiation, and termination sites of each uterine peristalsis wave. They got the same training on how to understand and read UPI images and passed the test using a sample dataset before reviewing the data in this work. The interobserver agreement evaluation was performed in 1240 uterine peristalses imaged using UPI from the first five participants across four phases in this study, the interobserver agreement was substantial with 0.93 intraclass correlation coefficients (ICC) in classifying UP directions, which indicates the great reliability and robustness across different observers. Two observers (A, B) had been intensively involved in research on ultrasound and MRI of nonpregnant uterus and are familiar with the topic. The other three observers (C, D, E) were biomedical engineers. All observers received the same instructions on how to assess the endometrial waves. All UPI activation movies were masked for patients' name, demographics, OBGYN history, and menstrual phase. All UPI videos were independently inspected by observers C, D, and E. If the observers disagreed on the direction or initiation or termination site of a uterine wave, A and B examined the movie and made the final call. Next, the software automatically calculated the duration, magnitude, and power of each uterine peristalsis wave. Finally, we performed statistical analysis of the uterine peristalsis wave frequency, direction ratio, and mean value of duration, magnitude, and power.

Inspection of TVUS images
Three registered sonographers were invovled in the independent reviews (without knowledge of the UPI results) of the TVUS recordings to determine the uterine peristalsis direction. They are specialized in the field of OBGYN, with experience in watching TVUS images, and one of them had previously performed visual inspection of contractions for research. Only segments where all three sonographers reached a 100% agreement on the UP direction were utilized to validate our UPI findings acquired simultaneously during TVUS.

Electrophysiological characterization and quantification
Three UPI electrophysiological indices were defined to qualitatively and quantitatively describe uteirne peristalsis patterns. Duration (Sec.) was defined as the duration of a complete peristalsis wave measured in the isochrone map (Fig. 2A) of the uterine peristalsis wave. Magnitude (mV) was defined as the average peak amplitude of electrical potential over the uterine region experiencing activation during the entire peristalsis wave. A magnitude map (Fig. 2B) was developed to present the magnitude distribution over the entire 3D uterine surface in one peristalsis. Power (mV*sec) was defined as the product of magnitude and duration for each uterine peristalsis wave.

Spatial and temporal analysis of human uterine peristalsis
Frequency was determined by counting the number of uterine peristalsis waves detected during the recording session and dividing it by the total imaging time. To analyze the compositions of uterine peristalsis propagation direction, initiation, and termination sites (Fig. 2C–E), we calculated the number of peristalsis waves with specific propagation directions (F–C, C–F, or other) and initiation and termination sites (cervical, fundal, or other regions). These counts were then divided by the total

number of peristalsis waves observed during the 30-min electrical mapping session.

The direction ratio (Fig. 2C) represents the percentage of peristalsis waves occurring in each direction out of the total number of peristalsis waves observed. Initiation and termination sites were identified as the regions where uterine peristalsis started and ended, respectively, based on the activation sequences. These sites were categorized into three groups: Cervical region, Fundal region, and Other regions. The initiation (termination) site composition (Fig. 2D–E) denotes the percentage of peristalses initiated (terminated) in each uterine region (cervical, fundal, or other region) throughout the entire recording.

To determine the initiation or termination probability for each point in each direction, we calculated the relative frequency measurement (ranging from 0 to 1) by dividing the number of peristalsis waves initiated or terminated at a specific point by the total number of peristalsis waves in that direction during the imaging session. This allowed us to generate spatial probability maps of initiation or termination sites (Fig. 2F–G) on the uterine surface.

Statistical analysis

Baseline demographic and OBGYN history characteristics of patients were summarized by using frequencies and percentages for categorical variables and means (95% confidence interval) for OBGYN history, ovarian follicles, and hormone measurements.

The primary outcomes of each uterine peristalsis wave were one qualitative variable (direction) and three quantitative variables: duration (sec), magnitude (mV), and power (mV*sec). UPI-indexed parameters were calculated according to directions (C–F, F–C, and others) using the mean value of UPI measurements for each patient in each visit within the standard 30-min time window. Kruskal-Wallis test was performed to analyze the difference of each UPI parameter between menstrual cycle phases. $P < 0.05$ was considered statistically significant.

DATA AVAILABILITY

The data reported in this work are available from the corresponding author upon reasonable request.

REFERENCES

1. Kuijsters, N. P. M. et al. Uterine peristalsis and fertility: current knowledge and future perspectives: a review and meta-analysis. *Reprod. BioMed. Online* **35**, 50–71 (2017).
2. de Vries, K., Lyons, E. A., Ballard, G., Levi, C. S. & Lindsay, D. J. Contractions of the inner third of the myometrium. *Am. J. Obstet. Gynecol.* **162**, 679–682 (1990).
3. Lyons, E. A. et al. Characterization of subendometrial myometrial contractions throughout the menstrual cycle in normal fertile women. *Fertil. Steril.* **55**, 771–774 (1991).
4. Bulletti, C. et al. Uterine contractility during the menstrual cycle. *Hum. Reprod.* **15**, 81–89 (2000).
5. Kunz, G. & Leyendecker, G. Uterine peristaltic activity during the menstrual cycle: characterization, regulation, function and dysfunction. *Reprod. Biomed. Online* **4**, 5–9 (2002).
6. Kuijsters, N. P. M. et al. Validation of electrohysterography for uterine peristalsis in non-pregnant uteri. *Fertil. Steril.* **100**, S383 (2013).
7. Kuijsters, N. P. M. et al. Propagation of spontaneous electrical activity in the ex vivo human uterus. *Pflugers Arch. Eur. J. Physiol.* **472**, 1065–1078 (2020).
8. Bulletti, C. et al. Abnormal uterine contractility in nonpregnant women. in *Annals of the New York Academy of Sciences* **828** 223–229 (1997).
9. Bulletti, C. & de Ziegler, D. Uterine contractility and embryo implantation. *Curr. Opin. Obstet. Gynecol.* **17**, 265–276 (2005).
10. Duquette, R. A. et al. Vimentin-positive, c-KIT-negative interstitial cells in human and rat uterus: a role in pacemaking? *Biol. Reprod.* **72**, 276–283 (2005).
11. Ijland, M. M. et al. Endometrial wavelike movements during the menstrual cycle. *Fertil. Steril.* **65**, 746–749 (1996).
12. van Gestel, I., IJland, M. M., Evers, J. L. H. & Hoogland, H. J. Complex endometrial wave-patterns in IVF. *Fertil. Steril.* **88**, 612–615 (2007).
13. Kuijsters, N. P. M. et al. Visual inspection of transvaginal ultrasound videos to characterize uterine peristalsis: an inter-observer agreement study. *J. Ultrasound* **23**, 37–44 (2019).
14. Van Gestel, I., Ijland, M. M., Hoogland, H. J. & Evers, J. L. H. Endometrial wave-like activity in the non-pregnant uterus. https://doi.org/10.1093/humupd/dmg011.
15. Ijland, M. M., Volovics, L., Evers, J. L. H., Hoogland, H. J. & Dunselman, G. A. J. Relation between endometrial wavelike activity and fecundability in spontaneous cycles. *Fertil. Steril.* **67**, 492–496 (1997).
16. Gora, S., Elad, D. & Jaffa, A. J. Objective analysis of vaginal ultrasound video clips for exploring uterine peristalsis post vaginal and cesarean section deliveries. *Reprod. Sci.* **25**, 899–908 (2018).
17. A, N. et al. Uterine peristalsis: comparison of transvaginal ultrasound and two different sequences of cine MR imaging. *J. Magn. Reson. Imaging* **20**, 463–469 (2004).
18. Forman, E. J. et al. Single embryo transfer with comprehensive chromosome screening results in improved ongoing pregnancy rates and decreased miscarriage rates. *Hum. Reprod.* **27**, 1217–1222 (2012).
19. Meirzon, D., Jaffa, A. J., Gordon, Z. & Elad, D. A new method for analysis of non-pregnant uterine peristalsis using transvaginal ultrasound. *Ultrasound Obstet. Gynecol.* **38**, 217–224 (2011).
20. Huang, Y. et al. Characterization of uterine peristaltic waves by ultrasound strain analysis. *IEEE Trans. Ultrason. Ferroelectr. Freq. Control* **69**, 2050–2060 (2022).
21. Huang, Y. Ultrasound-based strain mapping for quantitative characterization of uterine peristalsis outside pregnancy. at https://research.tue.nl/en/publications/ultrasound-based-strain-mapping-for-quantitative-characterization (2020).
22. Sammali, F. et al. Dedicated ultrasound speckle tracking for quantitative analysis of uterine motion outside pregnancy. *IEEE Trans. Ultrason. Ferroelectr. Freq. Control* **66**, 581–590 (2019).
23. Blank, C. et al. Assessment of uterine activity during IVF by quantitative ultrasound imaging: a pilot study. *Reprod. Biomed. Online* **41**, 1045–1053 (2020).
24. Rees, C. O. et al. Uterine contractile activity in healthy women throughout the menstrual cycle measured using a novel quantitative two-dimensional transvaginal ultrasound speckle tracking method. *Reprod. Biomed. Online* **46**, 115–122 (2023).
25. A, K. et al. Cine MR imaging of uterine peristalsis in patients with endometriosis. *Eur. Radiol.* **17**, 1813–1819 (2007).
26. Nakai, A. et al. Uterine peristalsis shown on cine MR imaging using ultrafast sequence. *J. Magn. Reson. Imaging* **18**, 726–733 (2003).
27. S, L. et al. Optimized approach to cine MRI of uterine peristalsis. *J. Magn. Reson. Imaging* **44**, 1397–1404 (2016).
28. Shitano, F. et al. Evaluation of uterine peristalsis using cine MRI on the coronal plane in comparison with the sagittal plane. *Acta radiol* **57**, 122–127 (2016).
29. Georgiou, J. et al. The electrouterograph: a novel tool for assessing uterine contractions of non-pregnant women. *IEEE Open J. Eng. Med. Biol.* **3**, 34–40 (2022).
30. Sammali, F., Kuijsters, N. P. M., Schoot, B. C., Mischi, M. & Rabotti, C. Feasibility of transabdominal electrohysterography for analysis of uterine activity in non-pregnant women. *Reprod. Sci.* **25**, 1124–1133 (2018).
31. Wu, W. et al. Noninvasive high-resolution electromyometrial imaging of uterine contractions in a translational sheep model. *Sci. Transl. Med.* **11**, eaau1428 (2019).
32. Wang, H. et al. Accuracy of electromyometrial imaging of uterine contractions in clinical environment. *Comput. Biol. Med.* **116**, 103543 (2020).
33. Wang, H. & Wang, Y. Spatial-dependent regularization to solve the inverse problem in electromyometrial imaging. *Med. Biol. Eng. Comput.* **58**, 1651–1665 (2020).
34. Cahill, A. G. et al. Analysis of electrophysiological activation of the uterus during human labor contractions. *JAMA Netw. Open* **5**, e2214707–e2214707 (2022).
35. Zhang, Y. et al. Analysis of in vivo uterine peristalsis in the non-pregnant female mouse. *Interface Focus* **9**, 20180082 (2019).
36. Eytan, O. et al. Characteristics of uterine peristalsis in spontaneous and induced cycles. *Fertil. Steril.* **76**, 337–341 (2001).
37. van Gestel, I., Ijland, M. M., Hoogland, H. J. & Evers, J. L. H. Endometrial wave-like activity in the non-pregnant uterus. *Hum. Reprod. Update* **9**, 131–138 (2003).
38. Ijland, M. M., Hoogland, H. J., Dunselman, G. A. J., Lo, C. R. & Evers, J. L. H. Endometrial wave direction switch and the outcome of in vitro fertilization. *Fertil. Steril.* **71**, 476–481 (1999).
39. Kunz, G., Beil, D., Deininger, H., Wildt, L. & Leyendecker, G. The dynamics of rapid sperm transport through the female genital tract: Evidence from vaginal

sonography of uterine peristalsis and hysterosalpingoscintigraphy. *Hum. Reprod.* **11**, 627–632 (1996).

40. Fanchin, R. et al. Uterine contractions at the time of embryo transfer alter pregnancy rates after in-vitro fertilization. *Hum. Reprod.* **13**, 1968–1974 (1998).

41. Lo, L. W. et al. An Inkjet-Printed PEDOT:PSS-Based Stretchable Conductor for Wearable Health Monitoring Device Applications. *ACS Appl. Mater. Interfaces* **13**, 21693–21702 (2021).

42. Lo, L. W. et al. Stretchable sponge electrodes for long-term and motion-artifact-tolerant recording of high-quality electrophysiologic signals. *ACS Nano* **16**, 11792–11801 (2022).

43. Wang, Y. & Rudy, Y. Application of the method of fundamental solutions to potential-based inverse electrocardiography. *Ann. Biomed. Eng.* **34**, 1272–1288 (2006).

44. Lammers, W. J. E. P., Ver Donck, L., Stephen, B., Smets, D. & Schuurkes, J. A. J. Focal activities and re-entrant propagations as mechanisms of gastric tachyarrhythmias. *Gastroenterology* **135**, 1601–1611 (2008).

45. Han, H., Cheng, L. K. & Paskaranandavadivel, N. High-resolution in vivo monophasic gastric slow waves to quantify activation and recovery profiles. *Neurogastroenterol. Motil.* **34**, e14422 (2022).

46. Paskaranandavadivel, N., Ogrady, G. & Cheng, L. K. Time delay mapping of high-resolution gastric slow wave activity. *IEEE Trans. Biomed. Eng.* **64**, 166 (2017).

47. Erickson, J. C. et al. Automated gastric slow wave cycle partitioning and visualization for high-resolution activation time maps. *Ann. Biomed. Eng.* **39**, 469–483 (2011).

48. O'Grady, G. et al. Origin and propagation of human gastric slow-wave activity defined by high-resolution mapping. *Am. J. Physiol. - Gastrointest. Liver Physiol.* **299**, 585–592 (2010).

AUTHOR CONTRIBUTIONS
S.W. and Y.W. designed the experiments and developed the UPI software. K.A., S.P., Q.W., V.R., and Y.W. contributed to the study design and guided the clinical studies. Q.W. and Y.W. developed the MRI sequence. S.W., K.A., S.P., and H.X. conducted human experiments. S.W. and H.X. segmented the MR images, S.P. reviewed the TVUS images. S.W. analyzed the data. S.W., K.A., S.P., V.R., Y.W. contributed to the manuscript writing.

COMPETING INTERESTS
The authors declare no competing non-financial interests but the following competing financial interests: Y.W. is a scientific consultant for Medtronic, EP solution, and has research fundings from NIH, Bill & Melinda Gates Foundation, and Burroughs Wellcome Fund.

ADDITIONAL INFORMATION
Supplementary information The online version contains supplementary material available at https://doi.org/10.1038/s44294-023-00003-x.

Correspondence and requests for materials should be addressed to Valerie Ratts or Yong Wang.

Reprints and permission information is available at http://www.nature.com/reprints

Publisher's note Springer Nature remains neutral with regard to jurisdictional claims in published maps and institutional affiliations.